12-2009

Microstructural Transformations And Kinetics Of High-Temperature Heterogeneous Gasless Reactions By High-Speed X-Ray Phase-Contrast Imaging

Robert V. Reeves
Purdue University

Jeremiah D.E. White
University of Notre Dame

Eric M. Dufresne
Argonne National Laboratory

Kamel Fezzaa
Argonne National Laboratory

Steven F. Son
Purdue University

See next page for additional authors

Recommended Citation
R. V. Reeves, S. F. Son, J. White, A. S. Mukasyan, E. M. Dufrensene and K. Fezzaa, "Microstructural Transformations and Kinetics of High-Temperature Heterogeneous Gasless Reactions by High-Speed X-ray Phase-Contrast Imaging," Physical Review B, Vol.80, iss.22, p. 224103, 2009. dx.doi.org/10.1103/PhysRevB.80.224103

Authors
Robert V. Reeves, Jeremiah D.E. White, Eric M. Dufresne, Kamel Fezzaa, Steven F. Son, Arvind Varma, and Alexander S. Mukasyan

Microstructural transformations and kinetics of high-temperature heterogeneous gasless reactions by high-speed x-ray phase-contrast imaging

Robert V. Reeves,[1] Jeremiah D. E. White,[2] Eric M. Dufresne,[3] Kamel Fezzaa,[3] Steven F. Son,[1] Arvind Varma,[4] and Alexander S. Mukasyan[2]

[1]*School of Mechanical Engineering, Purdue University, West Lafayette, Indiana 47907, USA*

[2]*Department of Chemical and Biomolecular Engineering, University of Notre Dame, Notre Dame, Indiana 46556, USA*

[3]*X-Ray Science Division, Argonne National Laboratory, 9700 South Cass Avenue, Argonne, Illinois 60439, USA*

[4]*School of Chemical Engineering, Purdue University, West Lafayette, Indiana 47907, USA*

(Received 27 August 2009; revised manuscript received 30 October 2009; published 7 December 2009)

Heterogeneous gasless reactive systems, including high-energy density metal-nonmetal compositions, have seen increasing study due to their various applications. However, owing to their high reaction temperature, short reaction time, and small scale of heterogeneity, investigation of their reaction mechanisms and kinetics is very difficult. In this study, microstructural changes and the kinetics of product layer growth in the W-Si system was investigated using a high-speed x-ray phase-contrast imaging technique. Using the Advanced Photon Source of Argonne National Laboratory, this method allowed direct imaging of irreversible reactions in the W-Si reactive system at frame rates up to 36 000 frames per second with 4 μs exposure and spatial resolution of 10 μm. Details of the Si melt and reactions between W and Si, that are unable to be viewed with visible-light imaging, were revealed. These include processes such as the initiation of nucleated melting and other physical phenomena that provide insight into the mixing of reactants and subsequent reaction. Through the use of this imaging technique and future optimization in the imaging process, a model for accurately identifying kinetics of chemical reactions, both spatially and temporally, is also proposed.

DOI: 10.1103/PhysRevB.80.224103 PACS number(s): 07.85.Qe, 81.70.−q, 82.33.Vx

I. INTRODUCTION

The high-energy release rate of composite energetic materials is useful in many applications, such as explosives, propellants, and materials synthesis. While most of these processes depend on the production of gas-phase products, reactions occurring in high-energy density gasless composite reactive systems have recently received significant interest.[1–8] These systems remain in the condensed state during reaction and are characterized by having a short interaction time (0.1–100 μs), a small scale of heterogeneity (0.01–100 μm) and high transient temperature growth rates (10^4–10^6 K/s). Only quantification of the progressive changes in the microstructure of the reactive system can allow for selection of the appropriate kinetic model, as well as reveal aspects of the microstructural instabilities induced by high rates of heating and chemical reaction. In the above context, it is clear that the inherent characteristics of these gasless reactive systems make investigation of their reaction kinetics and microstructural transformations a difficult task.

Owing to their highly penetrating nature, x rays have been used since their discovery as a nondestructive technique for imaging internal structures of objects. Low-brilliance sources, however, can require long exposure times to generate a high-contrast image. Producing single images can take from seconds up to minutes,[9] so such sources are not useful to study rapidly reacting or quickly moving systems. On the other hand, third-generation synchrotron radiation sources provide enough brilliance to permit imaging with high temporal resolution. Previous work has shown that it is possible to image systems using exposure times in the millisecond[10,11] to submicrosecond[12] time scales. Recently, time-resolved imaging as short as 150 ps has been demonstrated at the Advanced Photon Source (APS) of Argonne National Laboratory using white undulator radiation and stroboscopic detection.[13] This technique provides extremely high-quality data for repeating or cyclical events. Efforts have also been used successful in performing diffraction experiments with time resolution on the order of 100 fs.[14–17] Imaging irreversible phenomena occurring over the time scales of phase transitions, such as melting and rapid reactions in high-energy density gasless systems, however, requires capturing the evolution of the full process over time durations of up to a second. In the case of the previously discussed techniques, this would require collection of up to millions of images, leading to extremely expensive and time-consuming experiments.

Using x-ray imaging for small length scales presents its own challenges. X-ray imaging methods based on absorption techniques have low effectiveness at small length scales. Contrast due to x-ray absorption can be weak, especially for low-density materials and at higher x-ray energies, whereas contrast due to phase shift in these conditions can still be significant.[18–21] This makes phase-contrast radiography more effective at imaging small-scale materials, low-density materials, or materials with small density variations.

Third-generation synchrotrons are able to provide high-brilliance x rays with very high spatial coherence. Previous work has demonstrated that high spatial coherence can allow for a simple method of phase-contrast imaging using in-line transmission geometry.[9,10,22–25] By utilizing the third-generation synchrotron at the APS as an undulator radiation source, a simple in-line experimental geometry utilizing phase contrast can be used to perform a time-resolved study of the internal structure of a reactive system.

In this work, a procedure for directly visualizing the kinetics of product layer growth in a high-energy density gas-

less reactive system is introduced. Utilizing x-ray phase-contrast imaging in an in-line transmission configuration, a high-speed microimaging system was constructed at the 7-ID beamline at APS and used to investigate the high-temperature reaction kinetics of the W-Si system. By imaging at frame rates as high as 36 000 frames per second (fps) with integration times as low as 4 μs, the details of the W-Si reactive system undergoing high heating rates were investigated. Details of the Si melt and reactions between W and Si that cannot be viewed with visible-light imaging were revealed. These include processes such as the initiation of nucleated melting and other microscale physical phenomena that provide insight into the reactant mixing and kinetics of subsequent reactions.

II. METHOD

A. CAE setup

The computer-assisted electrothermography (CAE) experimental setup has been used previously to investigate the kinetics of chemical reactions in different heterogeneous systems.[26,27] In brief, a composite wire is placed between terminal blocks in the reaction chamber and is heated by passing electric current using a high-speed temperature controller. The temporal temperature profile for the wire can be preset and the computer program adjusts the input current as required to match the profile through a high-speed optical temperature sensor and feedback loop. Continuous, automated collection and processing of experimental data is also performed by the computer.

For these experiments, the test chamber was modified to allow for x-ray microimaging. Kapton windows were placed on either end of the chamber to allow for x-ray transmission through the test chamber with minimal absorption. Inert gas was slowly flowed steadily through the test chamber to provide a nonreactive environment. Helium gas was selected for its inertness, as well as its heat capacity to prevent any overshooting of the programmed temperature profile by the CAE device. The test chamber was also placed on an x-y adjustable stage to simplify alignment of the sample wire with the x-ray beam.

The temperature schedule was adapted to ease triggering of the camera and x-ray shutters. The x-ray shutter operates with a 30 ms delay, which was properly incorporated into the temperature profile timing. After the delay time elapsed, the CAE setup heated the wire at a prescribed rate, up to 2.5×10^5 K/s, until 2000 °C was reached. To make imaging more reliable, the test chamber was modified to spring load the terminal blocks, allowing the user to slightly pretension the test wire. Upon heating, the springs pull the wire taut, reducing the magnitude of wire oscillation caused by the rapid heating of the wire. Tensioning of the wire reduced the vibration to a magnitude smaller than the x-ray beam size, so unimpeded imaging of the wire from the onset of Si melt (1687 K) to closing of the x-ray shutter can be performed. Tests performed without pretension produced unusable results, as an $n=1$ vibration mode initiated with heating that caused the wire to oscillate at a magnitude much larger than the imaging window.

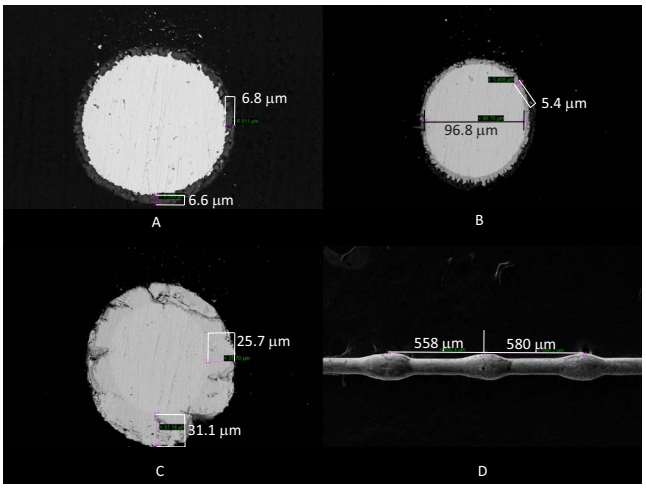

FIG. 1. (Color online) SEM images of unreacted and reacted wires. Figure A displays the unreacted 105 μm diameter W wire diameter with 6.6–6.8 μm Si layer. Figure B shows the reacted wire sectioned in between droplets. This section consists of a 96.8 μm W core with a WSi_2 product of thickness ~5.4 μm. Figure C shows the reacted wire sectioned at a droplet. The product layer in this section is a thicker layer of W_5Si_3 measuring 25.7–31.1 μm. Figure D shows the droplets as they solidified along the wire with the distance between them noted.

The clad wires used during the experimental testing were prepared by depositing a silicon layer of 5 μm thickness onto the initial W wire (Electronic Space Products International; 105 μm diameter, 99.97% purity). The deposition of Si was carried out in a silane argon gas mixture (4% SiH_4 and balance Ar) at silane partial pressure ~2 Torr and $T=873$ K, similar to the conditions previously used.[27] Microstructural analysis of the experimental samples was performed through scanning electron microscopy (SEM) (EVO 50 Series; Zeiss) imaging and energy dispersive x-ray spectroscopy (EDS) (INCAx-sight Model 7636; Oxford Instruments) analysis of both prereaction and postreaction materials. An SEM image of a typical wire is shown in Fig. 1(A), where the Si layer is clearly visible around a core of W. Figure 1(D) is an SEM image of the exterior of the wire after the experiment. Figures 1(B) and 1(C) are images of the cross-section of the postexperiment wire, with Fig. 1(B) taken at a location in between the large droplets and Fig. 1(C) taken inside one of the large droplets. Figures 1(B)–1(D) are discussed in more detail below. Inert wires of Ti with 100 μm diameter and of Mo and W, both with 127 μm diameter (Alfa-Aesar, Ward Hill, MA), were also used to test the imaging system at different photon energies, in order to optimize the exposure settings.

B. Imaging system

The basic design of the x-ray imaging setup is shown in Fig. 2. The experiments were carried out at 7-ID beamline of the APS. The x-ray source is the standard undulator A (33 mm period), and the energy spectrum of the white beam is defined by the undulator gap. It was set such that the main contribution to the image formation came from the first har-

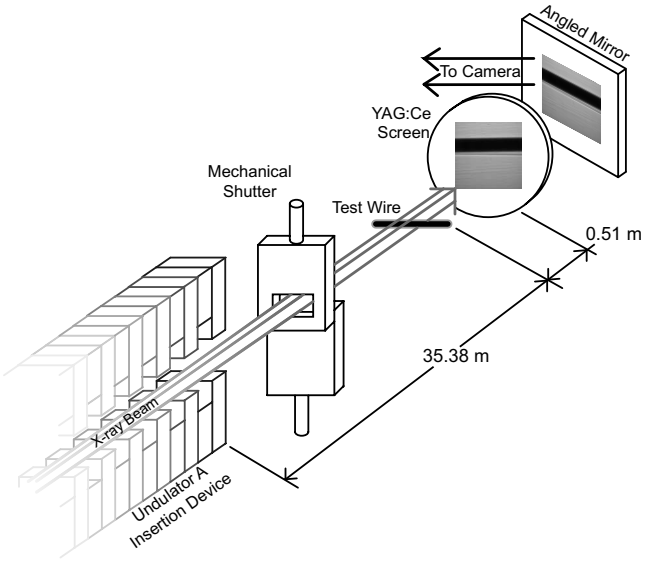

FIG. 2. Depiction of the x-ray imaging setup.

monic located at 13 keV. The beam passes through the preheated clad wire and impinges a cerium-doped yttrium aluminum garnet (YAG:Ce) scintillator, causing it to produce visible light at 550 nm. The scintillator is a bulk YAG:Ce crystal of 0.5 mm thickness. The produced light is reflected by a mirror and collected by a 10× Mitutoyo microscope objective attached to a Phantom v7.3 high-speed camera (Vision Research). The mirror is placed at a 45° angle to the beam to avoid placing the camera directly in line with the high-energy radiation.

A YAG:Ce crystal is used since it allows higher spatial resolution than other phosphors[28] and has been shown to handle the heat load associated with synchrotron radiation.[10,24] The visible fluorescence yield depends on the temperature of the screen, so to keep the measurement from becoming nonlinear, the screen must either be cooled or the duration of its exposure to x rays must be limited. It has been found that using a shutter in front of the YAG:Ce screen is an effective method to avoid nonlinear light production. This shutter has been described elsewhere[12] and is opened for a maximum duration of 200 ms.

The Phantom v7.3 is capable of imaging 5×10^5 fps with exposure times as low as 1 μs, although a typical frame rate of 36 000 fps with 4 μs exposure was used for the resolution required for these experiments. The Phantom v7.3 sensor is an 800×600 array with 22 micron pixels. After magnification by the 10× microscope objective, the effective pixel size of this setup is 2.2 μm. Images captured during experiments were processed using MATLAB and IMAGEJ image processing softwares.[29]

The nature of the reaction process has defined the experimental imaging area and experiment duration. Relatively long time scales (up to 100 ms) must be imaged in sequence to capture the irreversible nature of the gasless reaction and relatively large areas (500×500 μm^2 image size) must be examined to quantify the heterogeneity of the system during the phase transitions.

III. EXPERIMENTAL RESULTS

A. Experimental and theoretical intensity profiles

A computer code using the optical properties of a material, namely, the energy-dependent complex index of refraction, as well as the physical experimental parameters of propagation distances, source size, and full energy spectrum of the beam, was used to model the x-ray beam interaction with a coated wire of known size by utilizing the free-space Fresnel propagation approximation.[30] The code also takes into account the point-spread function (PSF) of the imaging system. The PSF of an imaging system can be envisioned as the impulse response of the system and describes the amount of blurring that occurs from imaging a point object. We measured it to be on the order of 10 μm full width at half maximum using the knife edge technique.[31]

The experimental data (images) are first normalized (flat fielded). This is a crucial step to ensure that the profile's variations are due to the sample and not to the features in the beam itself. We rely on these variations to identify a change in the local sample composition (Si and W mixture on the surface coating layer). Due to some instabilities inherent in the setup, the background image (the beam with no sample being imaged) drifts slightly in time. The correction procedure finds the best background match for each wire image, using local cross-correlation technique with a large number of background images. Next, a path line is described in IMAGEJ and the intensity values of the normalized image along this path line are recorded. The intensity values are rescaled based on the background intensity, and the profile plots and simulations are spatially normalized to the wire radii.

B. CAE results

The recorded data from the CAE setup for a typical experiment is shown in Fig. 3, which shows the temperature, T, and heat release rate, q, dependences versus time. The temperature profile shows that the heating rate yields the programmed temperature profile of increasing the temperature from 1000 to 2000 °C at a rate of 2.5×10^5 °C/s. The heat release rate profile also reveals important information about the reaction and its progress. The negative values of q from time $t=52$ to 55 ms indicate that the melting of Si occurs during this 3 ms window. The sharp spike to a large positive value of q indicates that the reaction between W and Si has begun. The reaction continues until q returns to zero, about 7 ms later. After this time, the power input to the wire is equal to the heat losses and the temperature remains constant.[26,27]

C. Time correlation between CAE and imaging system

To temporally correlate the captured images with the recorded CAE data, the latter is examined to find the time at which the applied voltage exceeds the threshold of the trigger. After this time is identified, the images captured from the camera and the data from the CAE setup can be temporally aligned. During the heating stage of the W-Si wires, melting of the Si layer was accurately recorded and the corresponding frames are shown in Fig. 3. The elapsed time between Fig. 3(A), the onset of heating, and Fig. 3(B), where

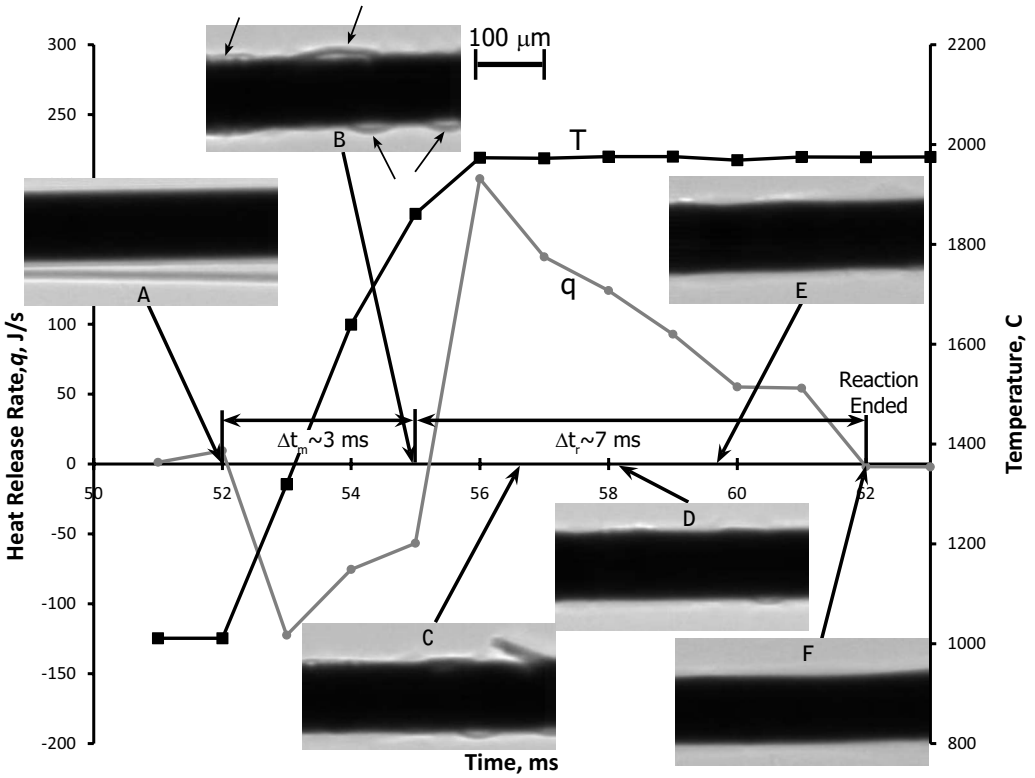

FIG. 3. Plot of heat release rate, q, and wire temperature, T versus time. The data shows that the Si melt occurs over a period of ~3 ms. The reaction is seen to conclude within ~10 ms of the onset of heating. The inset images show the evolution of the W-Si reaction with their temporal location indicated by arrows. Melt nucleation sites are distinguished by arrows in figure B. These sites grow, coalesce, and disperse evenly along the periphery of the wire. As the reaction progresses, the bright fringe, seen at the edge of the wire in figure A, decreases in intensity.

the bulk of Si is melted, is 3.053 ms. This correlates well to the CAE data shown in Fig. 3 (~3 ms of melting time). However, the images show that this melting process is a complex event and requires a more detailed description than is available from the CAE data.

D. Initial silicon melt

The initial condition of the wire, as shown in Fig. 3(A), is solid Si coating a W core. In this image, a strand of Si has detached from the wire along its bottom edge. After the temperature of the Si reaches its melting temperature (~1414 °C), several arches of solid Si are seen to form at the surface in Fig. 3(B). Video images show the melt initiates nearly simultaneously at many distinct points along the wire. The melt nucleates are indicated in Fig. 3(B) by arrows. The dark arches are strands of solid Si that have an area of melt underneath them. The Si melt effectively detaches the solid Si from the W wire and thermal stresses cause the arch to extend away from the wire. These areas expand as more Si melts, as shown in Fig. 3(C), which occurs 4.441 ms after heating begins. Shortly after, the Si melt consumes the solid Si arches, shown in Fig. 3(C), and is spread evenly across the wire, illustrated in Figs. 3(D) and 3(E) at times 6.106 and 7.771 ms after heating, respectively.

Although the CAE data indicates the melt is complete within ~3 ms of the onset of heating, Fig. 3(B) shows that some solid Si still remains, forming the dark arches. This is a detail of the melting process that direct imaging is able to describe in more detail than the CAE apparatus. In fact, the CAE data cannot explicitly describe the completion of melting and the onset of reaction, as these events temporally overlap. The crossover point in q, which is generally taken to be the completion of the melt, is actually the time at which the reaction begins to release heat at a faster rate than the melting Si can absorb it. However, the images are able to show the existence of solid Si after the q crossover. Images show the final identifiable solid Si melts at a time 5.300 ms after heating, a difference of 2.300 ms when compared to the CAE results. This region is seen on the bottom of the wire depicted in Fig. 3(C). The nonhomogenous form of the melting process, both in its initiation at discrete points and in the persistence of solid Si at local regions, is not discernible using conventional kinetic measurement system, but is easily described by the high-speed x-ray imaging technique.

A sharp diffraction fringe at the wire's entire periphery is also seen in Figs. 3(A) and 3(B). In subsequent frames, the fringe intensity decreases around much of the wire, with it located only in small regions in Fig. 3(E). These regions are magnified in Fig. 4's inset. The decrease in size and intensity of the fringe can be explained through modeling the wire's phase image. Figure 4 shows both experimental and simulated intensity profiles taken in a radial direction. By comparing intensity values for progressive images in this plot, the intensity of the experimental wire's fringe is seen to de-

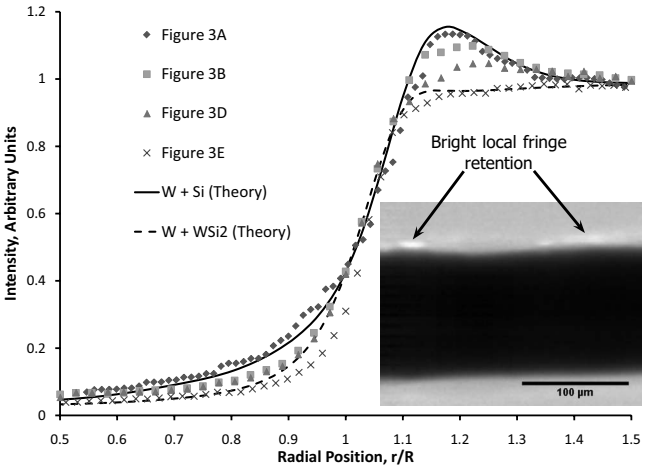

FIG. 4. Intensity profile in the radial direction for a W-Si composite wire undergoing reaction, where R is the wire's outer radius. The depletion in fringe intensity with time is related to the progress of reaction in the wire.

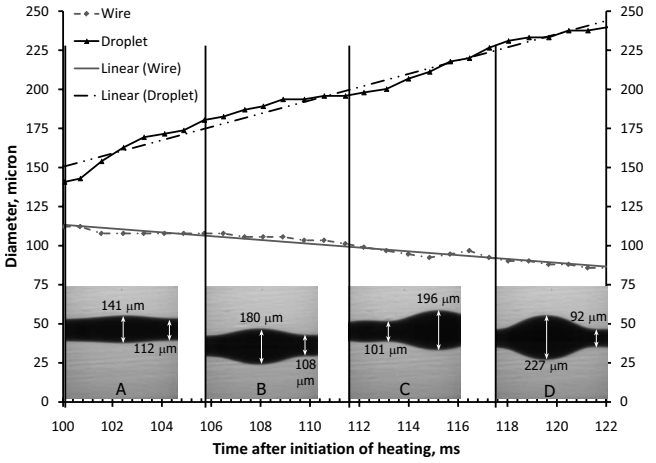

FIG. 5. Growth of droplet due to formation of W_5Si_3 product. Image A is taken at time $t=100.053$ ms after onset of heating. Images B, C, and D are taken at $t=105.742$, 111.486, and 117.256 ms, respectively.

crease with time. For comparison, simulations of the wire with an outer coating of unreacted Si and with a WSi_2 product layer were overlayed on the experimental data. The simulation with unreacted Si matches well with the initial wire profile and the simulation with WSi_2 correlates well with the measured data from the final frame. From this, it is understood that the loss of fringe intensity is related to the progress of reaction. Therefore, it can be inferred that in regions which maintain a bright fringe, the reaction has not yet progressed. Based on the images and this analysis, the reaction does not take place uniformly along the wire, but instead occurs in discrete areas which then expand to consume the rest of the reactants, similarly to the formation and growth of the Si melt.

E. Reaction progression

The Si melt seen in Fig. 3 is quickly consumed in a chemical reaction. The CAE data in Fig. 3 indicates that this reaction is completed within ~10 ms of the initial melt. The video images show a free moving surface on the wire, suggesting that the outer layer of reaction products is liquid. The eutectic of WSi_2 is 2030 °C, so if this layer remains liquid, it implies that the actual temperature of the wire is above the temperature indicated by the CAE apparatus (1987 °C). Some error is to be expected, and this level of error (2% of range) is common to this method.[32] Since this product remains liquid, the reaction is not limited by diffusion through a solid disilicide layer and rapidly proceeds to completion. *Thus, it was shown by in situ experiments, that the investigated system's reaction mechanism at these temperatures can be defined by direct metal dissolution in liquid Si*. This finding contradicts the conventionally accepted mechanism which assumes reagent diffusion through the layer of solid product.[33] It is more important that this dissolution-crystallization route explains unusually high rates of chemical interaction in this gasless system at these temperatures.

Much later (near $t=100$ ms), the unexpected phenomena of large liquid instabilities are seen to form along the wire with regular spacing, as seen in Fig. 1(D). Figure 5 shows four x-ray images representing droplet growth and a plot showing the size of a droplet with respect to time. It should be noted that this wire configuration provides a W-rich reaction environment. The outer diameter of the W wire that would remain after complete consumption of free Si available in the wire in the initial reaction $W+2Si \rightarrow WSi_2$ is calculated to be ~97 μm. In Fig. 5, the measured minimum outer diameter of the wire plus reaction products (<90 μm) is well below this calculated value. Also, the interdroplet distance required to form between uniformly spaced droplets of the observed size from the calculated volume of available WSi_2 is calculated to be about 900 μm, which is significantly higher than the 558–580 μm measured in Fig. 1(D). Thus, redistribution of the initial product phase (WSi_2) is unable to develop the structure seen in Fig. 1(D). This suggests that a secondary reaction takes place after the initial reaction, forming more liquid products and causing more frequent appearance of the droplets.

In the W-Si system, after the reaction forming WSi_2 is complete through consumption of free Si, a secondary reaction between W and WSi_2 forming W_5Si_3 occurs, although at a slower rate than the initial reaction, as studied elsewhere.[33–35] This is in accordance with the binary W-Si phase diagram,[36] and the progression of reactions is presented in Table I. Existence of the W_5Si_3 phase was verified through EDS analysis of the reacted wire. It is interesting to note that the thin product layer between droplets, as seen in Fig. 1(B), consists mainly of WSi_2, while the droplets' product layer, shown in Fig. 1(C), is made up of W_5Si_3. When the distance between uniformly spaced droplets is recalculated with the droplets made solely of W_5Si_3 and the interdroplet regions being WSi_2, the predicted frequency becomes 590 μm, which is close to the observed values.

A striking characteristic of this layer is its mobility along the wire. As the wire oscillates, the droplets are seen to oscillate as well. This droplet motion helps to damp out the motion of the wire caused by the high heating rates. The fluid motion makes it clear that both initial and secondary reaction

TABLE I. Chemical compositions and reactions at 2000 °C based on atomic percentage of W.

Atomic percentage, W	Reaction (Ref. 36)	Physical process seen in images
0 to 33.3%	$W+2Si \rightarrow WSi_2$	Nucleated Si melt Dissolution of W into Si
33.3% to end of test (<62.5 % W)	$WSi_2+W \rightarrow W_5Si_3$	W diffusion into WSi_2 Large droplet formation

products are liquid. The regular size and location of the droplets is also due to their liquid composition. Their formation is explained through the Rayleigh instability.[37] As sufficient amounts of W_5Si_3 form on the wire, droplets form in order to minimize the surface area. The density difference between the two reaction products ($\rho_{W_5Si_3}=14.42$ g/cm^3, $\rho_{WSi_2}=9.82$ g/cm^3) forces the less dense WSi_2 into the space between the resulting droplets. This process is visible in the collected movies. Smaller droplets are seen to merge with larger droplets. This behavior suggests the Rayleigh instability as the motive force for fluid motion along the wire, rather than any sort of capillary effects caused by minor oscillations of the wire.

By taking linear intensity profiles through the droplets, it is possible to determine the chemical composition of the droplets and verify the occurrence of the secondary reaction. Figure 6 shows radial intensity profiles taken from two locations in Fig. 5(D). Figure 6(A) depicts a profile through the large drop and Fig. 6(B) depicts one through the narrow portion of the wire. In addition to the experimental profiles, simulated intensity profiles are included for different product layer materials: unreacted Si, the initial-reaction product WSi_2 and the secondary-reaction product W_5Si_3. The physical dimensions used in the simulations were taken from Figs. 2(B), 2(C), and 5(D). The simulation in Fig. 6(A) for the large droplet (diameter=227 μm) using secondary-reaction products shows the best correlation to the experimental data, verifying the existence of W_5Si_3 in the droplets. The simulated profiles in Fig. 6(B) for the narrow wire using WSi_2 and W_5Si_3 as outer layer material provide similar results to each other. Since the resolution of the optical system is near 10 μm and the product layer for this portion of the wire is ~5.4 μm, the model is unable to distinguish between them. So, if the optical system's resolution is high enough, it is possible to identify product layer composition from analyzing the intensity response in these images.

The collected x-ray images not only show that a secondary reaction takes place at large scales in this system but also provides information about the rate of reaction. This information cannot be extracted from the CAE data. The lower exothermicity of the secondary reaction results in less heat generation and, coupled with low rate of the reaction, masked its existence in the CAE data. However, through analysis of the collected images, we are able to identify the occurrence of the secondary reaction and identify chemical composition of the forming droplets. Thus, this method of x-ray phase-contrast imaging allows direct measurement of the kinetics of a high-temperature heterogeneous reaction, as well as determination of the resulting product species.

IV. CONCLUSIONS

The dynamic response of a gasless reactive system under high heating rates has been studied using the high-speed x-ray phase-contrast imaging technique. The technique's characteristics at an undulator source such as APS, namely, a high spatial resolution on the order of 10 μm and the ability to view internal structures with exposures as low as 4 μs, provide the ability to monitor aspects of reacting systems

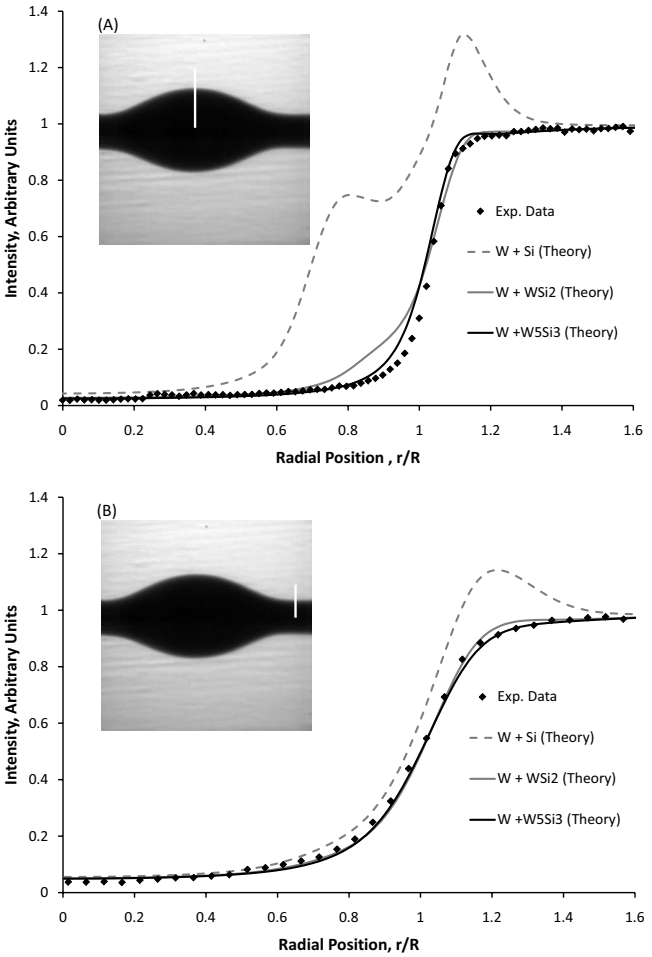

FIG. 6. Intensity plots taken in the radial direction in (A) a large droplet and (B) the narrow wire, as seen in the inset. By adjusting the material properties to account for different chemical compositions, the appropriate material can be selected by selecting the best fitting modeled profile. In figure (B), the results for the modeling of $W+WSi_2$ and $W+W_5Si_3$ are almost indistinguishable since the resolution of the optical system is larger than the product layer that is being modeled.

that cannot be viewed with visible-light imaging. In particular, the melting process for the Si coating of the bimetallic wire was found to initiate discretely at high heating rates, rather than uniformly from the inner surface of the Si. The nucleated nature of the melt's formation and evolution has effects in the reactions which are to follow. Besides melting, other events that can affect the kinetics of the chemical reaction, such as microscale physical phenomena, which provide insight into the mixing and reaction process, can be monitored at relevant time scales.

A method for spatially and temporally locating individual chemical phases has also been developed. We have compared and shown strong correlation between experimental and theoretical intensity profiles for samples containing multiple chemical species, when the resolution of the optical system is high enough and is properly modeled. In this system, monitoring the location of depleted diffraction fringes allowed us to find discrete regions of reaction, indicating that the reactions in the W-Si system occurred nonuniformly along the surface of the composite wire. The reaction initiated at distinct points and then spread along the wire to consume free Si, rather than acting as a purely diffusive process moving outward from the W-Si interface. A secondary reaction was also monitored and positively identified through this method. The ability to correlate intensity profiles to chemical composition raises the possibility of directly measuring time-resolved chemical-composition variations in materials through reconstruction of the object from the collected phase-contrast images.

Improvements of the resolution characteristics are also possible in future work. By changing from a bulk YAG:Ce crystal to a thin YAG:Ce or cerium-doped lutetium yttrium orthosilicate (LYSO) screen, increasing the magnification of the microscope objective, or utilizing higher energy x rays, overall spatial resolution may be improved. Future upgrades to the APS beamline as well as advances in complementary metal-oxide semiconductor cameras could also lead to submicrosecond time resolution. These enhancements will yield substantial benefits in the understanding of high-energy density reactions through direct optical measurements of reaction kinetics.

ACKNOWLEDGMENTS

S. Kharatyan is acknowledged for his help with utilizing the CAE setup in these experiments. Also, J. Wang is acknowledged for helpful discussions regarding the design of the optical system in these experiments. Use of the Advanced Photon Source at Argonne National Laboratory was supported by the U.S. Department of Energy, Office of Science, Office of Basic Energy Sciences, under Contract No. DE-AC02-06CH11357. This work was funded by the Office of Naval Research under Contract No. N0014-07-1-0969 with Clifford Bedford as the Program Manager.

[1] J. P. McDonald, V. C. Hodges, E. D. Jones, and D. P. Adams, Appl. Phys. Lett. **94**, 034102 (2009).
[2] A. S. Mukasyan and A. S. Rogachev, Prog. Energy Combust. Sci. **34**, 377 (2008).
[3] A. S. Rogachev, Usp. Khim. **77**, 21 (2008).
[4] S. F. Son, T. J. Foley, V. E. Sanders, A. M. Novak, D. G. Tasker, and B. W. Asay, in *Symposium on Multifunctional Energetic Materials*, 2005 MRS Fall Meeting, Boston, MA, 2005, edited by N. N. Thadhani, R. W. Armstrong, A. E. Gash, and W. H. Wilson, (MRS, Pittsburgh, 2006), p. 87.
[5] S. L. Kharatyan and A. A. Chatilyan, Combust., Explos. Shock Waves **36**, 342 (2000).
[6] E. L. Dreizin, Prog. Energy Combust. Sci. **35**, 141 (2009).
[7] S. F. Son, B. W. Asay, T. J. Foley, R. A. Yetter, M. H. Wu, and G. A. Risha, J. Propul. Power **23**, 715 (2007).
[8] A. Varma, V. Diokov, and E. Shafirovich, AIChE J. **51**, 2876 (2005).
[9] S. C. Mayo, T. J. Davis, T. E. Gureyev, P. R. Miller, D. Paganin, A. Pogany, A. W. Stevenson, and S. W. Wilkins, Opt. Express **11**, 2289 (2003).
[10] M. Di Michiel, J. M. Merino, D. Fernandez-Carreiras, T. Buslaps, V. Honkimaki, P. Falus, T. Martins, and O. Svensson, Rev. Sci. Instrum. **76**, 043702 (2005).
[11] S. V. Tipnis, V. V. Nagarkar, V. Gaysinskiy, S. R. Miller, and I. Shestakova, IEEE Trans. Nucl. Sci. **49**, 2415 (2002).
[12] Y. J. Wang, X. Liu, K. S. Im, W. K. Lee, J. Wang, K. Fezzaa, D. L. S. Hung, and J. R. Winkelman, Nat. Phys. **4**, 305 (2008).
[13] K. C. Lin, C. Carter, K. Fezzaa, J. Wang, and Z. Liu, *47th AIAA Aerospace Sciences Meeting and Exhibit* (AIAA, Orlando, FL, 2009), Vol. 2009.
[14] P. Beaud *et al.*, Phys. Rev. Lett. **99**, 174801 (2007).
[15] L. Bocklage, B. Kruger, R. Eiselt, M. Bolte, P. Fischer, and G. Meier, Phys. Rev. B **78**, 180405 (2008).
[16] F. S. Krasniqi, S. L. Johnson, P. Beaud, M. Kaiser, D. Grolimund, and G. Ingold, Phys. Rev. B **78**, 174302 (2008).
[17] H. J. Lee *et al.*, Phys. Rev. B **77**, 132301 (2008).
[18] S. Lagomarsino, A. Cedola, P. Cloetens, S. DiFonzo, W. Jark, G. Soullie, and C. Riekel, Appl. Phys. Lett. **71**, 2557 (1997).
[19] K. A. Nugent, T. E. Gureyev, D. F. Cookson, D. Paganin, and Z. Barnea, Phys. Rev. Lett. **77**, 2961 (1996).
[20] A. Snigirev, I. Snigireva, V. Kohn, S. Kuznetsov, and I. Schelokov, Rev. Sci. Instrum. **66**, 5486 (1995).
[21] L. D. Turner, B. B. Dhal, J. P. Hayes, A. P. Mancuso, K. A. Nugent, D. Paterson, R. E. Scholten, C. Q. Tran, and A. G. Peele, Opt. Express **12**, 2960 (2004).
[22] B. D. Arhatari, A. P. Mancuso, A. G. Peele, and K. A. Nugent, Rev. Sci. Instrum. **75**, 5271 (2004).
[23] P. Cloetens *et al.*, *Fourth Biennial Conference on High Resolution X-Ray Diffraction and Topography (XTOP 98)*, Durham, England, 1998, J. Phys. D: Appl. Phys., special issue, **32** (10A), A145 (1999).
[24] F. García-Moreno, A. Rack, L. Helfen, T. Baumbach, S. Zabler, N. Babcsán, J. Banhart, T. Martin, C. Ponchut, and M. Di Michiel, Appl. Phys. Lett. **92**, 134104 (2008).
[25] C. Raven, A. Snigirev, I. Snigireva, P. Spanne, A. Souvorov, and V. Kohn, Appl. Phys. Lett. **69**, 1826 (1996).

[26] A. Pelekh, A. Mukasyan, and A. Varma, Rev. Sci. Instrum. **71**, 220 (2000).
[27] S. L. Kharatyan, H. A. Chatilyan, A. S. Mukasyan, D. A. Simonetti, and A. Varma, AIChE J. **51**, 261 (2005).
[28] Y. X. Wang, Francesco De Carlo, Derrick C. Mancini, Ian McNulty, Brian Tieman, John Bresnahan, Ian Foster, Joseph Insley, Peter Lane, Gregor von Laszewski, Carl Kesselman, Mei-Hui Su, and Marcus Thiebaux, Rev. Sci. Instrum. **72**, 2062 (2001).
[29] W. S. Rasband, U.S. National Institutes of Health (U.S. National Institutes of Health, Bethesda, MA, 1997–2008), http://rsb.info.nih.gov/ij/
[30] M. Born and E. Wolf, *Principles of Optics*, 6th ed. (Pergamon, Oxford, 1980).
[31] E. M. Dufresne, D. A. Arms, N. R. Pereira, P. Ilinski, and R. Clarke, in *Eighth International Conference on Synchrotron Radiation Instrumentation (SRI 2003)*, edited by T. Warwick, J. Arthur, H. A. Padmore, and J. Stohr (Melville, San Francisco, CA, 2003), p. 780.
[32] Y. M. Grigorev, Y. R. Kolesov, and P. E. Chizhov, Instrum. Exp. Tech. **40**, 710 (1997).
[33] K. H. Lee, J. K. Yoon, J. K. Lee, J. M. Doh, K. T. Hong, and W. Y. Yoon, Surf. Coat. Technol. **187**, 146 (2004).
[34] R. W. Bartlett, P. A. Larssen, and P. R. Gage, Trans. Metall. Soc. AIME **230**, 1528 (1964).
[35] S. L. Kharatyan, H. A. Chatilyan, and A. B. Harutyunyan, in *Fifth International Conference on Diffusion in Materials*, Paris, France, 2000, edited by Y. Limoge and J. L. Bocquet (Scitec Publications, Uetikon-Zürich, 2001), p. 1557.
[36] *Binary Alloy Phase Diagrams*, T. Massalski, H. Okamato, P. Subramanian, and L. Kacprzak (ASM, Materials Park, OH, 1990).
[37] H. Liu, *Science and Engineering of Droplets, Fundamentals and Applications* (Noyes, Park Ridge, NJ, 2000).